

Resonant inelastic x-ray incarnation of Young's double-slit experiment

A. Revelli,¹ M. Moretti Sala,^{2,3} G. Monaco,⁴ P. Becker,⁵ L. Bohatý,⁵ M. Hermanns,^{6,7,8,9} T.C. Koethe,¹ T. Fröhlich,¹ P. Warzanowski,¹ T. Lorenz,¹ S.V. Streltsov,^{10,11} P.H.M. van Loosdrecht,¹ D.I. Khomskii,¹ J. van den Brink,¹² and M. Grüninger¹

¹*II. Physikalisches Institut, Universität zu Köln, Zùlpicher Strasse 77, D-50937 Köln, Germany*

²*European Synchrotron Radiation Facility, BP 220, F-38043 Grenoble Cedex, France*

³*Dipartimento di Fisica, Politecnico di Milano, Piazza Leonardo da Vinci 32, I-20133 Milano, Italy*

⁴*Dipartimento di Fisica, Università di Trento, via Sommarive 14, 38123 Povo (TN), Italy*

⁵*Abteilung Kristallographie, Institut für Geologie und Mineralogie, Zùlpicher Strasse 49b, D-50674 Köln, Germany*

⁶*Institut für Theoretische Physik, Universität zu Köln, Zùlpicher Strasse 77, D-50937 Köln, Germany*

⁷*Department of Physics, University of Gothenburg, SE-412 96 Gothenburg, Sweden*

⁸*Department of Physics, Stockholm University, AlbaNova University Center, SE-106 91 Stockholm, Sweden*

⁹*Nordita, KTH Royal Institute of Technology and Stockholm University, Roslagstullsbacken 23, SE-106 91 Stockholm, Sweden*

¹⁰*M.N. Miheev Institute of Metal Physics, Ural Branch,*

Russian Academy of Sciences, 620137 Ekaterinburg, Russia

¹¹*Ural Federal University, Mira Street 19, 620002 Ekaterinburg, Russia*

¹²*Institute for Theoretical Solid State Physics, IFW Dresden, Helmholtzstrasse 20, 01069 Dresden, Germany*

(Dated: January 18, 2019)

Young's archetypal double-slit experiment forms the basis for modern diffraction techniques: the elastic scattering of waves yields an interference pattern that captures the real-space structure. Here, we report on an inelastic incarnation of Young's experiment and demonstrate that *resonant inelastic* x-ray scattering (RIXS) measures interference patterns which reveal the symmetry and character of electronic excited states in the same way as elastic scattering does for the ground state. A prototypical example is provided by the quasi-molecular electronic structure of insulating $\text{Ba}_3\text{CeIr}_2\text{O}_9$ with structural Ir dimers and strong spin-orbit coupling. The double 'slits' in this resonant experiment are the highly localized core levels of the two Ir atoms within a dimer. The clear double-slit-type sinusoidal interference patterns that we observe allow us to characterize the electronic excitations, demonstrating the power of RIXS *interferometry* to unravel the electronic structure of solids containing, e.g., dimers, trimers, ladders, or other superstructures.

INTRODUCTION

RIXS provides a powerful example of particle-wave duality in quantum mechanics. In RIXS in the particle picture, an incident x-ray photon excites an electron out of the core of an atom into an empty valence level. The highly excited atomic state that is produced in this way contains an extremely localized hole in its core, with a size of a few pm. Subsequently this intermediate state decays: a valence electron fills the core hole under reemission of a photon with lower photon energy than the incident one. The final excited state may correspond to, e.g., an interband, orbital, or magnetic excitation [1]. Here, we focus on the equivalent picture of x-ray waves that are scattered via a localized intermediate state and interfere.

In the early 1990s it was realized that even if in RIXS the scattering is inelastic and the atomic core hole is very local, the amplitudes for its creation and annihilation have to be summed up *coherently* when identical ions are involved over which the *final* excited state is delocalized [2–4]. As a consequence, interference effects become possible. Specifically, in 1994 an interference pattern equivalent to Young's double-slit experiment was predicted for RIXS on diatomic molecules [3, 4], an effect that so far has not been observed. A double-slit-like interference occurs because the RIXS intermediate state contains a single core hole that can be on either of the two atoms in the molecule, see Fig. 1. The final state exhibits an electron in an excited molecular orbital which is delocalized over the two atoms. It corresponds to an observer with-

out 'which-path' information, i.e., one cannot tell on which atom the core hole was localized in the intermediate state. The emitted x-rays interfere and give rise to a double-slit-type sinusoidal interference pattern as a function of the momentum \mathbf{q} that is transferred in the inelastic scattering process.

In a gas of diatomic molecules, the interference is blurred by orientational disorder. This complication is absent in crystalline solids with a quasi-molecular electronic structure such

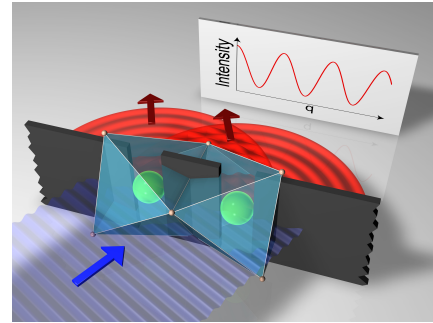


FIG. 1. Double-slit-type RIXS interferometry for an Ir_2O_9 bioc-tahedron. The incident plane wave (blue) resonantly excites a core electron on one of two equivalent Ir sites at \mathbf{r}_1 and \mathbf{r}_2 . This intermediate state decays to a quasi-molecular final state which is delocalized over both sites, i.e., without 'which-path' information. The emitted x-rays interfere with each other, giving rise to a double-slit-type sinusoidal interference pattern as a function of the transferred momentum \mathbf{q} which points along $\mathbf{r}_1 - \mathbf{r}_2$.

as insulating $\text{Ba}_3\text{CeIr}_2\text{O}_9$ (BCIO, see Fig. 2A) [5], an ideal model system with quasi-molecular orbitals localized on well-ordered structural dimers. As we show below, the excellent energy and momentum resolution of state-of-the-art RIXS [6] allows us to observe astonishingly clear interference patterns which are the unambiguous fingerprints of the symmetry of the low-energy electronic excitations.

RESULTS

We have grown single crystals of hexagonal BCIO (space group $P6_3/mmc$) by the melt-solution technique, see *Methods*. Each of the Ir^{4+} ions within the structural dimers formally shows a $5d^5$ configuration, with one hole in the t_{2g} shell. However, the nearest-neighbor Ir-Ir distance of 2.5 Å is even shorter than the 2.7 Å found in Ir metal. Accordingly, the intra-dimer Ir-Ir hopping is large, driving the formation of quasi-molecular orbitals with large bonding-antibonding splitting. It should be stressed that this situation is very different from the case of a single Ir^{4+} site, where strong spin-orbit coupling ($\lambda \approx 0.4 - 0.5$ eV) splits up the local t_{2g} manifold and yields spin-orbit-entangled $j = 1/2$ moments, see Fig. 2B. Prominent examples showing rich $j = 1/2$ physics are Sr_2IrO_4 [7–10] and Na_2IrO_3 [11–13].

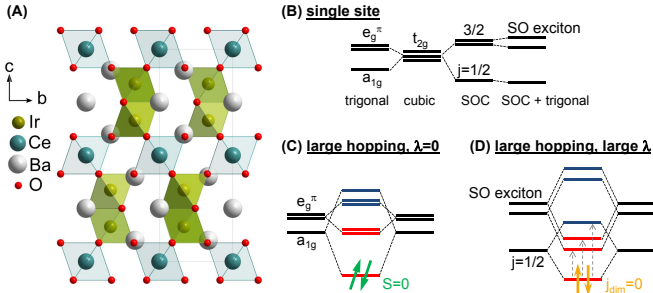


FIG. 2. Crystal structure and quasi-molecular orbitals of $\text{Ba}_3\text{CeIr}_2\text{O}_9$. (A) Layers of Ir_2O_9 biotahedra (light green) are sandwiched between Ce layers. The two Ir ions are displaced by 2.5 Å along c . (B) All sketches refer to the hole representation. For a single Ir^{4+} site, the t_{2g} level is split by a trigonal crystal field Δ_{CF} into a_{1g} and e_g^π orbitals or by spin-orbit coupling λ (SOC) into $j = 1/2$ and $3/2$ states. Real materials show both, λ and Δ_{CF} , which yields three distinct orbitals (right), where the two excited states are called spin-orbit exciton. (C,D) Sketches of quasi-molecular orbitals for two Ir^{4+} sites with dominant hopping and small Δ_{CF} . Bonding and antibonding levels [16, 17] are depicted in red and blue, respectively. In (C), $\lambda = 0$, as on the left hand side in (B). The ground state is the a_{1g}^2 spin singlet with total $S=0$ (green arrows). In (D), both spin-orbit coupling and hopping are large, as on the right hand side in (B). (Anti-)Bonding states are formed from local j states. The ground state is a total $j_{\text{dim}} = 0$ singlet built from two $j = 1/2$ states (orange arrows). Vertical dashed arrows indicate the 3 lowest excitations, which correspond to peaks α , β , and γ in the RIXS spectra. Rigorous calculations of the eigenstates (see methods and appendix) support that the simple picture plotted in (D) contains the essential character of the low-energy excitations.

There are two limiting scenarios for an effective description of the electronic structure of BCIO, i.e., for the character of the bonding and antibonding quasi-molecular orbitals. For strong spin-orbit coupling, (anti-) bonding states can be formed from spin-orbital $j = 1/2$ states, see Fig. 2D. However, a large Ir-Ir hopping may quench the $j = 1/2$ moments, as has been discussed for Na_2IrO_3 [14, 15]. In this case, the crystal-field-split t_{2g} orbitals provide a more appropriate basis for the formation of (anti-) bonding states, see Fig. 2C. As will become clear in the following, these substantial differences in the Ir $5d$ orbitals can be highlighted and quantified by RIXS interferometry, i.e., RIXS measurements of \mathbf{q} -dependent interference patterns which reveal the symmetry and character of the excited states.

Figure 3A depicts high-resolution RIXS spectra of BCIO for a fixed incident energy tuned to the Ir L_3 edge ($2p \rightarrow 5d$), see *Methods*, which resonantly enhances inelastic scattering from intra- t_{2g} excitations. With a $5d$ $t_{2g} - e_g^\sigma$ splitting of about 3 eV, the observed features between 0.5 eV and 1.5 eV, labeled α , β , and γ , can safely be attributed to intra- t_{2g} excitations. The absence of dispersion strongly supports a local character, see appendix. The spectra clearly do not display the characteristic feature of individual $j = 1/2$ moments, the narrow spin-orbit exciton peaking at about 1.5λ . A textbook

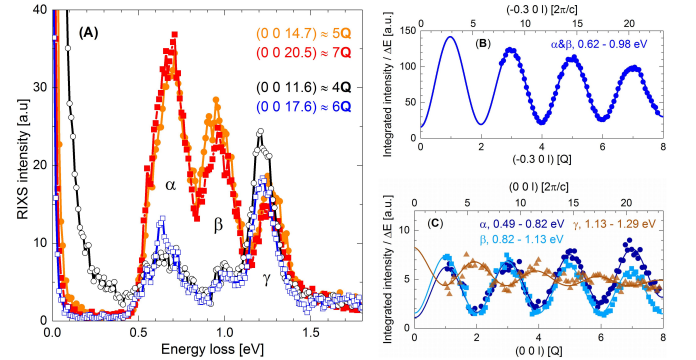


FIG. 3. RIXS data of intra- t_{2g} excitations in BCIO. (A) High-resolution RIXS spectra at $T = 20$ K for different transferred momenta $\mathbf{q} = (0 \ 0 \ mQ)$ with integer m and $Q = \pi/d = 2.914 \cdot 2\pi/c$, where d and c denote the intra-dimer Ir-Ir distance and the lattice constant, respectively. The spectra show a pronounced even/odd behavior with respect to m , reflecting the sinusoidal \mathbf{q} dependence. Note that the elastic peak is suppressed in π polarization for a scattering angle of $2\theta = 90^\circ$, and that the data for $4Q$ to $7Q$ were measured at $2\theta = 52^\circ, 67^\circ, 83^\circ$, and 101° , respectively. Accordingly, the elastic peak is strongest for $4Q$. (B,C) Interference patterns in the RIXS intensity as a function of \mathbf{q} . The data cover about 3.5 periods in Q , equivalent to more than 20 Brillouin zones (top axis). The intensity was integrated over the energy-loss ranges indicated in the figure and normalized by the width ΔE of the respective energy range. Data in (B) were measured at 10 K with lower energy resolution of 0.36 eV, integrating over features α and β , to enhance the signal-to-noise ratio. The high-resolution data in (C) discriminate between the three peaks α (dark blue), β (light blue), and γ (brown). Solid lines depict fits using $a_0 e^{-a_1 l} \cdot \sin^2(\pi l / 2Q + \varphi) + b_0 + b_1 l$ with the parameters Q , a_0 , a_1 , b_0 , and b_1 as well as $\varphi = 0$ or $\pi/2$.

example of the latter is found in isostructural $\text{Ba}_3\text{Ti}_{2.7}\text{Ir}_{0.3}\text{O}_9$, where the small Ir content prevents dimer formation, see appendix.

The crucial observation is that the integrated intensity of the observed features shows the characteristic two-beam interference pattern [3, 4], i.e., a pronounced sinusoidal oscillation as a function of q_c , the component of the transferred momentum \mathbf{q} parallel to the dimer axis, see Fig. 3B. The period $2Q = 2\pi/d$ yields $d = 2.530(8)$ Å at $T = 20$ K, in very good agreement with the Ir-Ir distance of $2.5361(7)$ Å determined at 300 K by x-ray diffraction, see appendix. Note that $Q = 2.914 \cdot 2\pi/c$ is incommensurate with the reciprocal lattice vector $2\pi/c$, where c denotes the lattice constant. A clear dichotomy with respect to even/odd Q is also evident from the RIXS spectra in Fig. 3A. Even without further knowledge of the underlying microscopic physics, the observed interference pattern with a period given by the Ir-Ir distance is an unmistakable proof of the double-slit-type RIXS process originating from the quasi-molecular orbital character of the investigated states.

DISCUSSION

The most remarkable feature of RIXS interferometry is the ability to determine the symmetry of the low-energy excitations and thus to distinguish between the two limiting scenarios sketched in Figs. 2C and 2D. The symmetry is encoded in the phase of the interference pattern. Young's canonical elastic double-slit experiment gives a maximum for $\mathbf{q}=0$, which is equivalent to the $\cos^2(qd/2)$ dependence observed for peak γ , see Fig. 3C. The cosine denotes the Fourier transform of the double slit, i.e., its structure factor. Strikingly, features α and β show a $\sin^2(qd/2)$ modulation. In our experiment on structural dimers with a bonding singlet ground state, the $\sin^2(qd/2)$ [$\cos^2(qd/2)$] behavior of the observed RIXS features reflects the bonding [antibonding] character of the corresponding excited-state wavefunctions. This behavior embodies the simple dipole selection rules for both the absorption and reemission processes, see appendix. The symmetry of the observed interference patterns agrees with Fig. 2D and suggests that this simplified sketch provides a valid starting point for an intuitive understanding of the three low-energy features α , β , and γ .

This assignment is corroborated by careful modeling of the Ir_2O_9 biotahedra. We take into account spin-orbit coupling λ , hopping terms within a dimer, the trigonal crystal field Δ_{CF} , and on-site Coulomb correlations described by Hubbard U and Hund exchange J_H , see *Methods*. The calculated RIXS spectra and the corresponding \mathbf{q} -dependent intensities (see Fig. 4) qualitatively agree with our experimental results. In particular, we reproduce the $\sin^2(qd/2)$ behavior of peaks α and β and the $\cos^2(qd/2)$ behavior of peak γ . This implies quasi-molecular orbitals that are governed by a combination of strong spin-orbit coupling $\lambda \approx 0.4-0.5$ eV and strong hopping ~ 1 eV. The hopping is about 3 times larger than between

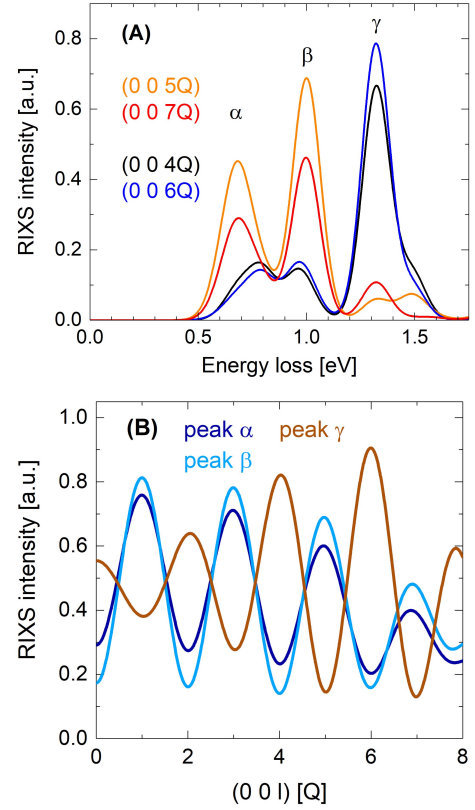


FIG. 4. **Calculated RIXS data of BCiO.** (A) Calculated RIXS spectra are plotted for the same \mathbf{q} values as the experimental data in Fig. 3, reproducing peaks α , β , and γ as well as their pronounced even/odd behavior with respect to Q (see appendix for more details). (B) \mathbf{q} -dependent interference patterns for peaks α , β , and γ , which have to be compared with the experimental result depicted in Fig. 3C. Parameters are $t_{a1g} = 1.1$ eV, $t_{e\pi} = 0.5$ eV, $U = 1.0$ eV, $J_H = 0.3$ eV, $\Delta_{\text{CF}} = -0.2$ eV, and $\lambda = 0.45$ eV (see appendix).

nearest-neighbor $j = 1/2$ moments in Sr_2IrO_4 . The dominant contribution to the ground state is a dimer singlet with $j_{\text{dim}} = 0$ in which the single-site $j = 1/2$ moments occupy a bonding quasi-molecular orbital. As depicted in Fig. 2D, the two lower features α and β correspond to excitations to bonding orbitals originating from the $j = 3/2$ spin-orbit exciton, their splitting is mainly caused by J_H and Δ_{CF} . We find that peak γ at 1.2 - 1.3 eV corresponds to the antibonding triplet excitation from the $j_{\text{dim}} = 0$ ground state to a $j_{\text{dim}} = 1$ excited state of a dimer. This j flip can be realized by both, spin-flip and spin-conserving processes. The former are allowed in L -edge RIXS due to the very strong spin-orbit coupling in the $2p$ shell in the intermediate state. In the calculated spectra the triplet excitation intensity is somewhat overestimated due to the neglect of the electron-hole continuum above the gap, which provides a possible decay channel for the local excitations considered here with a concomitant increase of the width.

Finally we address the envelope of the sinusoidal interference pattern. The RIXS data cover about 20 Brillouin zones. Still the amplitude of the intensity modulation does not change

strongly, at least for peaks α and β , allowing us to detect the interference pattern over a broad range of \mathbf{q} . This is due to the nearly point-like nature of the 'slits' formed by the core hole in the intermediate states [1], i.e., the 'slit width' is negligible. The \mathbf{q} -dependent envelope rather contains valuable information on the dependence of the RIXS matrix elements on the scattering geometry and thereby on the precise wave-functions.

CONCLUSION

The comparison of theory and experiment on BCIO shows that the quasi-molecular orbitals, delocalized over the two Ir sites of a dimer, give rise to the RIXS interference effect, which was predicted almost 25 years ago as an inelastic incarnation of Young's double-slit experiment. Conceptually different interference effects as a function of energy but not of q arise if *energetically* different intermediate states – located on the *same* site – contribute coherently [18, 19]. In contrast, our experiment realizes the genuine spatial double-slit setup: a photon scatters inelastically on one of two dimer sites. Previously, this was discussed in the context of dimers in VO₂ [20], but only a single value of q was analyzed due to the limited momentum transfer available in the soft x-ray range. Similarly, studies of magnons in the bilayer compound Sr₃Ir₂O₇ [21] and of stripes in nickelates and cuprates [22] addressed only a few values of q . Coverage of a broad range of q fully reveals the interference character and allowed us to unravel the symmetry and character of electronic dimer excitations in BCIO. These results demonstrate the potential of this interference method to probe the electronic structure of materials containing well-defined structural units such as dimers, trimers, or heptamers [23] as well as structures in which the carriers are 'localized' only in one direction, e.g., bilayers or ladders. More specifically, our results suggest that RIXS interferometry is ideally suited to explore the role of molecular orbitals in the spin-liquid candidate Ba₃InIr₂O₉ with In³⁺ ions and *three* holes per dimer [24] as well as to search for Majorana fermions in iridate candidates for a Kitaev spin liquid [9]. The latter quantum state lives on tricoordinated lattices, still spin correlations are restricted to nearest neighbors. Majorana fermion excitations are thus expected to show an interference pattern which is closely related to the case of dimers in BCIO. In general, RIXS interferometry will prove to be an efficient tool for studying the symmetry and character of excited states in complex materials.

MATERIALS AND METHODS

Crystal growth and characterization. The Ba₃MIr₂O₉ family with the hexagonal (6H)-BaTiO₃ structure is formed for a wide variety of di-, tri-, or tetravalent M ions [5, 25–27]. The valence states of $M = \text{Ce}^{4+}$ and Ti^{4+} yield $5d^5$ Ir⁴⁺ ions. Single crystals of Ba₃CeIr₂O₉ and Ba₃Ti_{2.7}Ir_{0.3}O₉ have been

grown by the melt-solution technique and spontaneous nucleation. Using stoichiometric amounts of BaCO₃, CeO₂, and IrO₂ for the growth of Ba₃CeIr₂O₉ and BaCO₃, TiO₂, and IrO₂ in a ratio of 3 : 2 : 1 in the case of Ba₃Ti_{2.7}Ir_{0.3}O₉, and in both cases an addition of BaCl₂ · 2H₂O, hexagonal prismatic crystals of about 2 mm size were grown within growth periods of four weeks. The crystals were mechanically separated from the flux, washed with cold H₂O, and characterized by x-ray diffraction, energy-dispersive x-ray (EDX) analysis, and magnetization measurements.

RIXS measurements. RIXS measurements at the Ir L_3 edge were performed on the ID20 beamline at ESRF [6]. We used an incident energy of 11.2155 keV for $M = \text{Ce}$ and 11.2150 keV for $M = \text{Ti}$ to maximize the resonantly enhanced RIXS intensity of the intra- t_{2g} excitations. An overall energy resolution of 27 meV was obtained by combining a Si(844) back-scattering monochromator and $R = 2$ m Si(844) spherical diced crystal analyzers [28]. These analyzers make the RIXS setup partially dispersive, i.e., one image on the pixelated detector covers an energy range of approximately 360 meV. Accordingly, the RIXS spectra of Fig. 3A were measured by scanning the energy at constant \mathbf{q} while the data in Fig. 3C were collected by scanning \mathbf{q} at constant energy. The data in Fig. 3B were measured with a lower resolution of 0.36 eV using a Si(311) channel-cut in place of the Si(844) back-scattering monochromator in order to enhance the signal-to-noise ratio. For both $M = \text{Ce}$ and Ti , RIXS measurements were performed on polished (0 0 1) surfaces with the c axis in the horizontal scattering plane and the a axis along the vertical direction. The incident photons were π polarized. Samples were cooled using a continuous-flow He cryostat.

Theory. The sketch in Fig. 2D provides a simplified but intuitive picture of the low-energy excitations. For the simulation of the RIXS spectra, we calculate all 66 eigenstates for two t_{2g} holes on two Ir sites of an Ir₂O₉ bioctahedron via exact diagonalization. We start from the Hamiltonian for a single Ir site, taking into account spin-orbit coupling $\lambda \mathbf{S} \cdot \mathbf{L}$ and the trigonal crystal field, $\Delta_{\text{CF}} L_z^2$. The on-site Coulomb repulsion between carriers with different spins in the same or in different orbitals is given by U and $U - 2J_H$, respectively, and the interaction Hamiltonian reads

$$H_C = U \sum_{i,\alpha} n_{i\alpha\uparrow} n_{i\alpha\downarrow} + \frac{1}{2} (U - 3J_H) \sum_{i,\sigma,\alpha \neq \alpha'} n_{i\alpha\sigma} n_{i\alpha'\sigma} \\ + (U - 2J_H) \sum_{i,\alpha \neq \alpha'} n_{i\alpha\uparrow} n_{i\alpha'\downarrow} \\ + (U - 2J_H) \sum_i \left(15 - 5 \sum_{\alpha,\sigma} n_{i\alpha\sigma} \right),$$

where $n_{i\alpha\sigma}$ is the number operator for the t_{2g} orbitals $\alpha \in \{a_{1g}, e_g^{\pi+}, e_g^{\pi-}\}$ [17] at site i with $\sigma \in \{\uparrow, \downarrow\}$. Additionally, we consider the hopping interactions $t_{a_{1g}}$ and $t_{e_g^{\pi}}$ between two Ir sites.

The two octahedra forming an Ir₂O₉ bioctahedron are rotated by 180° with respect to each other around the trigonal z

axis, see Fig. 2(A) and Fig. S1 in the appendix. This causes a sign change of the xz and yz orbitals in one of the two octahedra, which affects the selection rules of excitations involving the e_g^π orbitals [17]. For the calculation of the RIXS spectra, we consider the RIXS matrix elements for single-particle excitations between all 66 states in the dipole approximation for both absorption and reemission. As typical for t_{2g}^5 iridates [29], we neglect multiplet effects between the intermediate-state $2p_{3/2}$ core hole and $5d$ holes, which significantly simplifies the calculation. It is motivated for a t_{2g}^5 configuration by the full t_{2g} shell in the intermediate state, neglecting the e_g^σ holes. Note, however, that spin-orbit coupling mixes e_g^π and e_g^σ levels. Moreover, this approximation is not fully valid for quasi-molecular orbitals delocalized over two Ir sites, where states with two holes on the same site contribute. For comparison with experiment, one has to add the RIXS intensities of the two layers of bioctahedra present in $\text{Ba}_3\text{CeIr}_2\text{O}_9$, see Fig. 2(A), which for the present geometry is equivalent to adding intensities for $+q$ and $-q$. Finally, RIXS spectra are calculated for certain q values by assuming Gaussian line shape with a fixed width.

Acknowledgments. We gratefully acknowledge fruitful discussions with M. Braden, I. Mazin, and S. Trebst. This project was funded by the Deutsche Forschungsgemeinschaft (DFG, German Research Foundation) – Project numbers 277146847 and 247310070 – CRC 1238 (projects A02, B01, B02, B03, and C02) and CRC 1143 (project A05), respectively. The work of S.V.S. was supported by the Russian Science Foundation through the project 17-12-01207.

-
- [1] L.J.P. Ament, M. van Veenendaal, T.P. Devereaux, J.P. Hill, J. van den Brink, *Resonant inelastic x-ray scattering studies of elementary excitations*, Rev. Mod. Phys. **83**, 705 (2011).
 - [2] Y. Ma, *X-ray absorption, emission, and resonant inelastic scattering in solids*, Phys. Rev. B **49**, 5799 (1994).
 - [3] Y. Ma, M. Blume, *Interference of fluorescence x rays and coherent excitation of core levels*, Rev. Sci. Instr. **66**, 1543 (1995).
 - [4] F. Gel'mukhanov, H. Agren, *Resonant inelastic x-ray scattering with symmetry-selective excitation*, Phys. Rev. A **49**, 4378 (1994).
 - [5] Y. Doi and Y. Hinatsu, *The structural and magnetic characterization of 6H-perovskite-type oxides $\text{Ba}_3\text{LnIr}_2\text{O}_9$ ($\text{Ln} = \text{Y}$, lanthanides)*, J. Phys.: Condens. Matter **16**, 2849 (2004).
 - [6] M. Moretti Sala, K. Martel, C. Henriquet, A. Al Zein, L. Simonelli, Ch.J. Sahle, H. Gonzalez, M.-C. Lagier, C. Ponchut, S. Huotari, R. Verbeni, M. Krisch, and G. Monaco, *A high-energy-resolution resonant inelastic X-ray scattering spectrometer at ID20 of the European Synchrotron Radiation Facility*, J. Synchrotron Rad. **25**, 580 (2018).
 - [7] B.J. Kim, H. Jin, S.J. Moon, J.-Y. Kim, B.-G. Park, C.S. Leem, J. Yu, T.W. Noh, C. Kim, S.-J. Oh, J.-H. Park, V. Durairaj, G. Cao, and E. Rotenberg, *Novel $J_{\text{eff}} = 1/2$ Mott State Induced by Relativistic Spin-Orbit Coupling in Sr_2IrO_4* , Phys. Rev. Lett. **101**, 076402 (2008).
 - [8] B.J. Kim, H. Ohsumi, T. Komesu, S. Sakai, T. Morita, H. Takagi, and T. Arima, *Phase-Sensitive Observation of a Spin-Orbital Mott State in Sr_2IrO_4* , Science **323**, 1329 (2009).
 - [9] J.G. Rau, E. Kin-Ho Lee, H.-Y. Kee, *Spin-Orbit Physics Giving Rise to Novel Phases in Correlated Systems: Iridates and Related Materials*, Annu. Rev. Condens. Matter Phys. **7**, 195 (2016).
 - [10] J. Kim, D. Casa, M.H. Upton, T. Gog, Y.-J. Kim, J.F. Mitchell, M. van Veenendaal, M. Daghofer, J. van den Brink, G. Khaliullin, and B.J. Kim, *Magnetic Excitation Spectra of Sr_2IrO_4 Probed by Resonant Inelastic X-Ray Scattering: Establishing Links to Cuprate Superconductors*, Phys. Rev. Lett. **108**, 177003 (2012).
 - [11] J. Chaloupka, G. Jackeli, G. Khaliullin, *Kitaev-Heisenberg Model on a Honeycomb Lattice: Possible Exotic Phases in Iridium Oxides A_2IrO_3* , Phys. Rev. Lett. **105**, 027204 (2010).
 - [12] V.M. Katukuri, S. Nishimoto, V. Yushankhai, A. Stoyanova, H. Kandpal, S. Choi, R. Coldea, I. Rousochatzakis, L. Hozoi, and J. van den Brink, *Kitaev interactions between $j = 1/2$ moments in honeycomb Na_2IrO_3 are large and ferromagnetic: insights from ab initio quantum chemistry calculations*, New J. Phys. **16**, 013056 (2014).
 - [13] H. Gretarsson, J.P. Clancy, X. Liu, J.P. Hill, E. Bozin, Y. Singh, S. Manni, P. Gegenwart, J. Kim, A.H. Said, D. Casa, T. Gog, M.H. Upton, H.-S. Kim, J. Yu, V.M. Katukuri, L. Hozoi, J. van den Brink, and Y.-J. Kim, *Crystal-Field Splitting and Correlation Effect on the Electronic Structure of A_2IrO_3* , Phys. Rev. Lett. **110**, 076402 (2013).
 - [14] I.I. Mazin, H.O. Jeschke, K. Foyevtsova, R. Valenti, and D.I. Khomskii, *Na_2IrO_3 as a Molecular Orbital Crystal*, Phys. Rev. Lett. **109**, 197201 (2012).
 - [15] K. Foyevtsova, H.O. Jeschke, I.I. Mazin, D.I. Khomskii, and R. Valenti, *Ab initio analysis of the tight-binding parameters and magnetic interactions in Na_2IrO_3* , Phys. Rev. B **88**, 035107 (2013).
 - [16] S.V. Streltsov, D.I. Khomskii, *Covalent bonds against magnetism in transition metal compounds*, Proc. Nat. Acad. Science **113**, 10491 (2016).
 - [17] D.I. Khomskii, K.I. Kugel, A.O. Sboychakov, S.V. Streltsov, *Role of Local Geometry in the Spin and Orbital Structure of Transition Metal Compounds*, J. Exp. Theo. Phys. **122**, 484 (2016).
 - [18] L.A. Wray, S.-W. Huang, Y. Xia, M.Z. Hasan, C. Mathy, H. Eisaki, Z. Hussain, and Y.-D. Chuang, *Experimental signatures of phase interference and subfemtosecond time dynamics on the incident energy axis of resonant inelastic x-ray scattering*, Phys. Rev. B **91**, 035131 (2015).
 - [19] A. Pietzsch, Y.-P. Sun, F. Hennies, Z. Rinkevicius, H.O. Karlsson, T. Schmitt, V.N. Strocov, J. Andersson, B. Kennedy, J. Schlappa, A. Föhlisch, J.-E. Rubensson, and F. Gel'mukhanov, *Spatial Quantum Beats in Vibrational Resonant Inelastic Soft X-Ray Scattering at Dissociating States in Oxygen*, Phys. Rev. Lett. **106**, 153004 (2011).
 - [20] H. He, A.X. Gray, P. Granitzka, J.W. Jeong, N.P. Aetukuri, R. Kukreja, L. Miao, S.A. Breitweiler, J. Wu, Y.B. Huang, P. Olalde-Velasco, J. Pelliciari, W.F. Schlotter, E. Arenholz, T. Schmitt, M.G. Samant, S.S.P. Parkin, H.A. Dürr, and L.A. Wray, *Measurement of collective excitations in VO_2 by resonant inelastic x-ray scattering*, Phys. Rev. B **94**, 161119(R) (2016).
 - [21] M. Moretti Sala, V. Schnells, S. Boseggia, L. Simonelli, A. Al-Zein, J.G. Vale, L. Paolasini, E.C. Hunter, R.S. Perry, D. Prabhakaran, A.T. Boothroyd, M. Krisch, G. Monaco, H.M. Rønnow, D.F. McMorrow, and F. Mila, *Evidence of quantum dimer excitations in $\text{Sr}_3\text{Ir}_2\text{O}_7$* , Phys. Rev. B **92**, 024405 (2015).
 - [22] W. Schülke and C. Sternemann, *Charge excitations in stripe-ordered $\text{La}_{5/3}\text{Sr}_{1/3}\text{NiO}_4$ and $\text{La}_{15/8}\text{Ba}_{1/8}\text{CuO}_4$: Interpretation*

- tion of the anomalous momentum transfer dependence via fluorescence interferometry, Phys. Rev. B **84**, 085143 (2011).
- [23] S.V. Streltsov, D.I. Khomskii, *Orbital physics in transition metal compounds: new trends*, Physics-Uspekhi **60**, 1121 (2017).
- [24] T. Dey, M. Majumder, J.C. Orain, A. Senyshyn, M. Prinz-Zwick, S. Bachus, Y. Tokiwa, F. Bert, P. Khuntia, N. Büttgen, A.A. Tsirlin, and P. Gegenwart, *Persistent low-temperature spin dynamics in the mixed-valence iridate $Ba_3IrIr_2O_9$* , Phys. Rev. B **96**, 174411 (2017).
- [25] T. Sakamoto, Y. Doi, and Y. Hinatsu, *Crystal structures and magnetic properties of 6H-perovskite-type oxides $Ba_3MIr_2O_9$ ($M = Mg, Ca, Sc, Ti, Zn, Sr, Zr, Cd$ and In)*, J. Sol. State Chem. **179**, 2595 (2006).
- [26] T. Dey, A.V. Mahajan, P. Khuntia, M. Baenitz, B. Koteswararao, and F.C. Chou, *Spin-liquid behavior in $J_{\text{eff}} = 1/2$ triangular lattice compound $Ba_3IrTi_2O_9$* , Phys. Rev. B **86**, 140405(R) (2012).
- [27] R. Kumar, D. Sheptyakov, P. Khuntia, K. Rolfs, P.G. Freeman, H.M. Rønnow, T. Dey, M. Baenitz, and A.V. Mahajan, *$Ba_3M_xTi_{3-x}O_9$ ($M = Ir, Rh$): A family of 5d/4d-based diluted quantum spin liquids*, Phys. Rev. B **94**, 174410 (2016).
- [28] M. Moretti Sala, C. Henriquet, L. Simonelli, R. Verbeni, and G. Monaco, *High energy-resolution set-up for Ir L_3 edge RIXS experiments*, J. Electron Spectrosc. Relat. Phenom. **188**, 150 (2013).
- [29] L.J.P. Ament, G. Khaliullin, and J. van den Brink, *Theory of resonant inelastic x-ray scattering in iridium oxide compounds: Probing spin-orbit-entangled ground states and excitations*, Phys. Rev. B **84**, 020403(R) (2011).
- [30] J. Rodríguez-Carvajal, *Recent advances in magnetic structure determination by neutron powder diffraction*, Physica B **192**, 55 (1993).
- [31] V. Petříček, M. Dušek, and L. Palatinus, *Crystallographic computing system JANA2006: General features*, Z. Kristallogr. **229**, 345 (2014).
- [32] M. Rossi, M. Retegan, C. Giacobbe, R. Fumagalli, A. Efimenko, T. Kulka, K. Wohlfeld, A.I. Gubanov, and M. Moretti Sala, *Possibility to realize spin-orbit-induced correlated physics in iridium fluorides*, Phys. Rev. B **95**, 235161 (2017).
- [33] Y. Sizyuk, C. Price, P. Wölfle, and N.B. Perkins, *Importance of anisotropic exchange interactions in honeycomb iridates: Minimal model for zigzag antiferromagnetic order in Na_2IrO_3* , Phys. Rev. B **90**, 155126 (2014).
- [34] B.H. Kim, G. Khaliullin, and B.I. Min, *Electronic excitations in the edge-shared relativistic Mott insulator: Na_2IrO_3* , Phys. Rev. B **89**, 081109(R) (2014).
- [35] J.P. Perdew, K. Burke, and M. Ernzerhof, *Generalized Gradient Approximation Made Simple*, Phys. Rev. Lett. **77**, 3865 (1996).

Appendix A: Crystal structure

The crystal structure of $Ba_3CeIr_2O_9$ was analyzed by x-ray diffraction measurements. Small crystals were ground to a fine powder which was studied on a D5000 diffractometer (Siemens) with Cu K_α radiation at 300 K. In order to calibrate the lattice constants, a small amount of Si powder was mixed with the sample. The lattice parameters were determined by Rietveld refinements with the software FullProf [30]. We find $a = b = 5.9035(9)$ Å and $c = 14.715(3)$ Å in good agreement

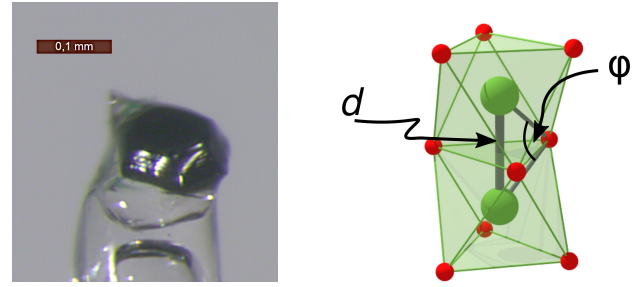


FIG. S1. Sample of $Ba_3CeIr_2O_9$ used for single-crystal x-ray diffraction (left) and sketch of an Ir_2O_9 bioctahedron with face-sharing octahedra (right). At 300 K, the Ir-Ir bond distance equals $d = 2.5361(7)$ Å and the Ir-O-Ir angle is $\varphi = 78.285(2)^\circ$.

with the powder diffraction analysis reported by Doi and Hinatsu [5].

The single-crystal diffraction experiment was performed on a Bruker AXS Kappa APEX II four-circle x-ray diffractometer with a wavelength of 0.71073 Å (Mo K_α). A non-spherical sample with a spatial extension of roughly 100 μm (see Fig. S1) was investigated at room temperature. Using a distance of 40 mm between detector and sample, we collected 94 002 reflections, of which 1 395 are unique. 1 241 of these reflections have an intensity significantly greater than zero. The absorption correction was carried out using a non-spherical model containing 25 faces and an absorption coefficient of $\mu = 48 \text{ mm}^{-1}$, yielding a weighted internal R value of $wR_2(\text{int}) = 5.8\%$. The structural model according to space group $P6_3/mmc$ (Nr. 194) with 17 structural parameters was refined using the software Jana2006 [31]. The refinement further includes an isotropic extinction correction. The structural refinement yields $R(F)$ values of $R(\text{obs}) = 4.37\%$, $wR(\text{obs}) = 6.06\%$, $R(\text{all}) = 5.01\%$, and $wR(\text{all}) = 6.14\%$. In the refinements we allowed for a shared occupation of the Ce and Ir sites with the constraint of full total occupation. However, the deviation of the refined occupation numbers from

	x	y	z	U_{iso} or U_{ani}
Ba(1)	0	0	1/4	0.00822(12)
Ba(2)	1/3	2/3	0.09993(4)	0.00970(11)
Ir	1/3	2/3	0.663825(17)	0.00400(7)
Ce	0	0	1/2	0.00388(11)
O(1)	0.1742(3)	0.8258(3)	0.5870(3)	0.0107(5)
O(2)	0.4857(4)	0.5143(4)	3/4	0.0052(5)

	U_{11}	U_{22}	U_{33}	U_{23}
Ba(1)	0.00917(15)	0.00917(15)	0.0063(2)	0.00458(7)
Ba(2)	0.00793(12)	0.00793(12)	0.0132(2)	0.00397(6)

TABLE S1. Structural parameters determined by x-ray diffraction. Positions are given in units of the cell parameters. The atomic isotropic or anisotropic displacement parameters U_{iso} , U_{ani} , and U_{ij} are given in Å². $U_{12} = U_{13} = 0$ Å² are constrained by symmetry.

the ideal ones are small and negative, namely $-0.029(12)$ for Ce on an Ir site and $-0.019(10)$ for Ir on a Ce site. There is thus no evidence for any disorder between Ce and Ir occupation. Only the atomic displacement parameters of the Ba atoms are refined anisotropically. The atomic positions and displacement parameters are listed in Table S1. The Ir-Ir bond distance amounts to $d = 2.5361(7)$ Å and the Ir-O-Ir angle to $\varphi = 78.285(2)^\circ$ (see Fig. S1), larger than the value of $\varphi_0 \approx 70.5^\circ$ expected for undistorted octahedra. Doi and Hinatsu [5] reported a similar value of $d = 2.5266(17)$ Å, also at room temperature.

Appendix B: RIXS on $\text{Ba}_3\text{Ti}_{2.7}\text{Ir}_{0.3}\text{O}_9$

The RIXS spectra of $\text{Ba}_3\text{Ti}_{2.7}\text{Ir}_{0.3}\text{O}_9$ show two narrow peaks at 0.57 eV and 0.70 eV, see Fig. S2. Considering the narrow line width, the comparably small splitting of 0.13 eV, and the insensitivity to the transferred momentum \mathbf{q} , the data of $\text{Ba}_3\text{Ti}_{2.7}\text{Ir}_{0.3}\text{O}_9$ are a textbook example of the spin-orbit excitation of individual $j = 1/2$ moments (in a non-cubic field), very similar to the case of iridium fluorides with strongly localized states [32] and very different from the dimer spectra observed in $\text{Ba}_3\text{CeIr}_2\text{O}_9$. This results from the small Ir content $x = 0.3$ with only 15 % of the bi-octahedral metal sites occupied by Ir^{4+} ions. The small value of x suppresses the formation of Ir_2O_9 units, thus nearest-neighbor Ir^{4+} ions are isolated in IrTiO_9 bi-octahedra. Based on a local crystal-field calculation [33], the two peak energies yield two possible solutions, either $\lambda = 0.40$ eV and a trigonal crystal field of $\Delta_{\text{trig}} = -0.23$ eV or $\lambda = 0.41$ eV and $\Delta_{\text{trig}} = +0.18$ eV. In the convention of our Hamiltonian, the negative sign of $\Delta_{\text{trig}} = -0.23$ eV agrees with the elongated octahedra found in x-ray diffraction. In hole notation, it corresponds to a lowering of the a_{1g} orbital, as depicted in Fig. 2.

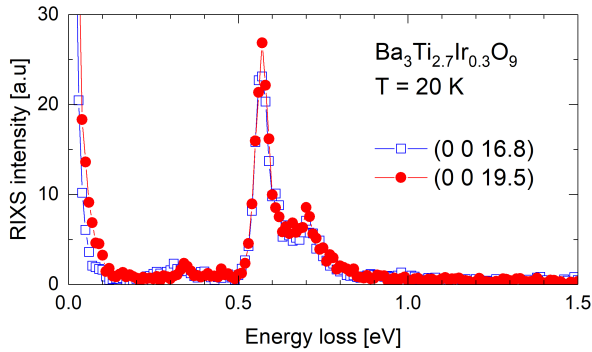


FIG. S2. **RIXS spectra of $\text{Ba}_3\text{Ti}_{2.7}\text{Ir}_{0.3}\text{O}_9$.** The small Ir content yields individual Ir^{4+} sites instead of dimers, showing a textbook example of the spin-orbit excitation, very different from the dimer spectra of $\text{Ba}_3\text{CeIr}_2\text{O}_9$.

Appendix C: Absence of significant dispersion

The scenario of local dimers is well supported by the absence of any significant dispersion upon variation of the transferred momentum parallel or perpendicular to c , see Fig. S3. The strong change of intensity upon variation of \mathbf{q} parallel to c (bottom panel) agrees with the data shown in Fig. 3 of the main text, it reflects double-slit interference. In contrast, the small monotonic change of intensity of feature β at 1 eV observed for changing \mathbf{q} perpendicular to c (top panel) can be attributed to matrix element effects, i.e., to polarization and experimental geometry.

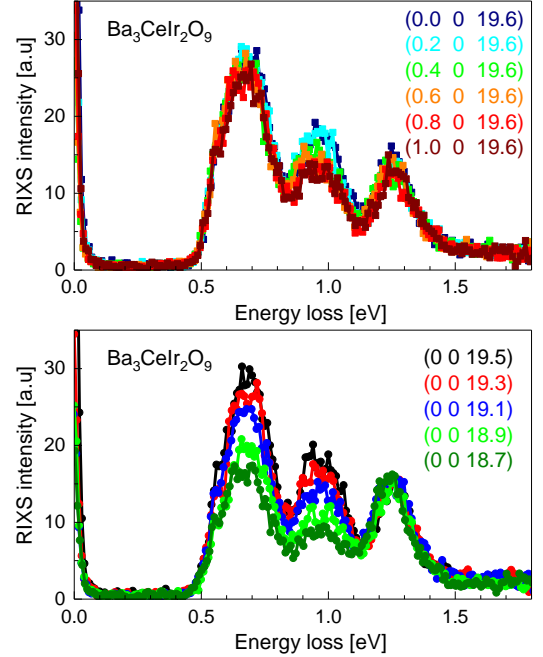


FIG. S3. **Absence of dispersion in the RIXS spectra.** The three RIXS features do not show any significant dispersion upon variation of the transferred momentum either parallel (bottom) or perpendicular (top) to c .

Appendix D: Momentum-dependence of double-slit-type RIXS

The sinusoidal \mathbf{q} dependence is obtained in a straightforward way by considering the RIXS intensity $I(\mathbf{q}, \omega) = \sum_f |A_f(\mathbf{q})|^2 \delta(\hbar\omega - E_f)$ for the excited states $|f\rangle$ with energy E_f . In dipole approximation, the amplitude $A_f(\mathbf{q})$ reads [29]

$$A_f(\mathbf{q}) \propto \langle f | \sum_{\mathbf{R}} e^{i\mathbf{q}\cdot\mathbf{R}} [D^\dagger(\varepsilon_{\text{out}}^*) D(\varepsilon_{\text{in}})]_R | 0 \rangle$$

where $|0\rangle$ denotes the ground state, ε_i the polarization of incident and scattered photons, D the local dipole transition operator, and \mathbf{R} runs over all Ir sites that contribute to a given final state $|f\rangle$. In the present case with quasi-molecular orbitals

within a biotetrahedron, these are the two crystallographically equivalent Ir sites at $\mathbf{r}_{1,2} = (0, 0, \pm d/2)$. For these two sites, the matrix elements may only differ in sign. For $\mathbf{q} \parallel \mathbf{r}_2 - \mathbf{r}_1$, the even and odd combinations $[D^\dagger D](e^{i\mathbf{q}\mathbf{r}_1} \pm e^{i\mathbf{q}\mathbf{r}_2})$ yield [3]

$$A_f^+(q) \propto \cos(qd/2) \langle f | [D^\dagger(\varepsilon_{\text{out}}^*) D(\varepsilon_{\text{in}})] | 0 \rangle,$$

$$A_f^-(q) \propto \sin(qd/2) \langle f | [D^\dagger(\varepsilon_{\text{out}}^*) D(\varepsilon_{\text{in}})] | 0 \rangle,$$

which explains the observed \mathbf{q} dependence, in particular the period $2Q = 2\pi/d$ in the intensity.

A precise determination of electronic parameters is beyond the scope of this study, but we consider the parameters used in the main text as very reasonable. Our values for the intra-orbital $U = 1.0$ eV, $J_H = 0.3$ eV, $\lambda = 0.45$ eV, and $\Delta_{\text{CF}} = -0.2$ eV lie well within the accepted range for iridates [34]. In the convention of our Hamiltonian, the negative sign of Δ_{CF} corresponds to the situation depicted in Fig. 2, where the a_{1g} orbital is lowered in the hole picture. For an estimate of the hopping parameters, we performed band-structure calculations in the generalized gradient approximation (GGA) [35]. These calculations yield $t_{a_{1g}} \approx 0.9$ eV and $t_{e_g^\pi} \approx 0.3$ eV. We used $t_{a_{1g}} = 1.1$ eV and $t_{e_g^\pi} = 0.5$ eV for the simulation of the RIXS data, in reasonable agreement with the prediction. Small deviations may partially be caused by neglecting the empty e_g^σ orbitals, which is the typical approach for $5d^5$ iridates. Both, spin-orbit coupling and Coulomb correlations give rise to a finite mixing of e_g^π and e_g^σ orbitals, affecting the effective hopping parameter. Furthermore, our simplified two-site model neglects oxygen states and the electron-hole continuum, impeding a full quantitative description of the RIXS spectra.

Appendix E: Substructure of the three RIXS features

Figure 2D of the main text is a simplified sketch which, however, provides an appropriate description of the essential physics for the low-energy excitations discussed here. As an example, consider the following ground-state wavefunction obtained from the comparison of experiment and theory, i.e.,

using the parameters given in Fig. 4 of the main text,

$$\begin{aligned} \Psi_0 \approx & \alpha \left| \frac{1}{2}, \frac{1}{2} \right\rangle \left| \frac{1}{2}, -\frac{1}{2} \right\rangle \\ & + \beta \left[e^{i\frac{\pi}{2}} \left| \frac{1}{2}, \frac{1}{2} \right\rangle \left| \frac{3}{2}, \frac{3}{2} \right\rangle + e^{-i\frac{\pi}{2}} \left| \frac{1}{2}, -\frac{1}{2} \right\rangle \left| \frac{3}{2}, -\frac{3}{2} \right\rangle \right] \\ & + \gamma \left[e^{i\frac{\pi}{4}} \left| \frac{1}{2}, \frac{1}{2} \right\rangle \left| \frac{3}{2}, \frac{1}{2} \right\rangle - e^{-i\frac{\pi}{4}} \left| \frac{1}{2}, -\frac{1}{2} \right\rangle \left| \frac{3}{2}, -\frac{1}{2} \right\rangle \right] \\ & + \delta \left[\left| \frac{1}{2}, \frac{1}{2} \right\rangle \left| \frac{3}{2}, -\frac{1}{2} \right\rangle + \left| \frac{1}{2}, -\frac{1}{2} \right\rangle \left| \frac{3}{2}, \frac{1}{2} \right\rangle \right] \\ & + \epsilon \left[e^{-i\frac{\pi}{4}} \left| \frac{1}{2}, \frac{1}{2} \right\rangle \left| \frac{3}{2}, -\frac{3}{2} \right\rangle - e^{i\frac{\pi}{4}} \left| \frac{1}{2}, -\frac{1}{2} \right\rangle \left| \frac{3}{2}, \frac{3}{2} \right\rangle \right]. \end{aligned}$$

All terms refer to bonding (i.e., even) combinations of $|j, j_z\rangle |j', j'_z\rangle$ with $\alpha = 0.82$, $\beta = 0.23$, $\gamma = -0.27$, $\delta = 0.02$, and $\epsilon = 0.17$. Terms with amplitude < 0.01 are omitted for clarity. The strongly dominant value of α supports the picture sketched in Fig. 2D of the main text.

The three features in the experimental RIXS spectrum are composed of several related excitations which are slightly split by the interplay of Coulomb interactions, crystal field, and spin-orbit coupling. Figure S4 resolves the individual excitations, using the same parameters as in the main text and a reduced Gaussian width. The experimentally unresolved substructure gives rise to an asymmetric line shape and causes small changes of shape and energy of the experimental features as a function of q . Overall, the character of the experimentally resolved excitations is well approximated by Fig. 2D.

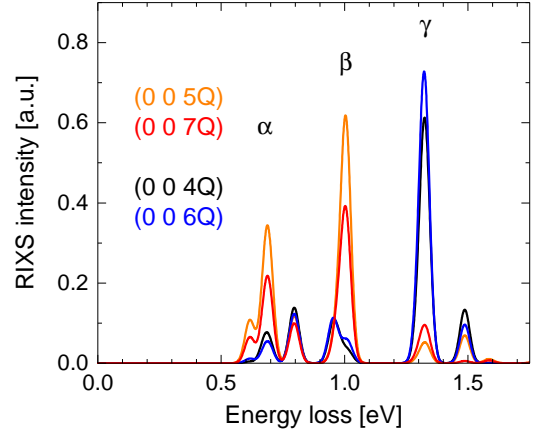


FIG. S4. **RIXS spectra calculated with reduced width.** Parameters are the same as in Fig. 4 of the main text, only the Gaussian width has been reduced.